SUPERPARAMAGNETIC $ZnFe_2O_4$ NANOPARTICLES: THE EFFECT OF Ca AND Gd DOPING

Marcella Bini[a,*], Christian Tondo[a], Doretta Capsoni[a], Maria Cristina Mozzati[b], Benedetta Albini[b] and Pietro Galinetto[b]

[a] Dept. of Chemistry, University of Pavia, viale Taramelli 16, 27100 Pavia Italy;

[b] Dept. of Physics and CNISM, University of Pavia, via Bassi 6, 27100 Pavia, Italy;

Corresponding Author

Marcella Bini, Dept. of Chemistry, University of Pavia, viale Taramelli 16, 27100 Pavia Italy;

e-mail: bini@unipv.it

Abstract

$ZnFe_2O_4$ ferrite nanoparticles are arousing a great interest in the biomedical field, in particular for magnetic hyperthermia application, thanks to their superparamagnetic behaviour at room temperature. In order to better tuning the magnetic properties, different doping substitution and synthesis methods have been tried to reduce particle sizes and to vary the cation distribution on the spinel sites. In this paper, we focused on the microwave combustion synthesis method of Ca (on Zn site) and Gd (on Fe site) substituted ferrites. Undoped $ZnFe_2O_4$ and Sr and Al doped samples were also synthesized for comparison. The use of X-ray powder diffraction, microscopic and spectroscopic techniques allowed us to ensure the good quality of the spinel structure for all the investigated samples, to determine a homogeneous distribution of the dopants and an average particle size lower than 11 nm. In addition, we estimated the inversion degree of the spinels by using the Rietveld structural refinement and Raman spectroscopy. By means of SQUID magnetometry we found, for all the samples, a superparamagnetic behaviour with saturation magnetization between 6 and 10 emu/g at the maximum applied magnetic field of 3T, with a more effective role played by Ca ions with respect to Gd ions substitution.

Keywords: $ZnFe_2O_4$; X-ray diffraction; Micro-Raman; Magnetization; Superparamagnetic effect; Doping.

1. Introduction

The increasing interest towards iron oxides and ferrite nanoparticles is justified by their unique physico-chemical properties due to the quantum confinement, if compared to bulk materials, when the particle sizes are lower than about 30 nm [1-4]. These properties lead to a superparamagnetic behaviour [5] and make them good candidates for different medical applications, e.g. for either diagnosis or therapy, as magnetic resonance imaging (MRI) contrast agents and for radiofrequency magnetic hyperthermia (MH).[1] Recently, it has been also evidenced the possibility to engineer theranostic systems in which both of these applications are integrated in the same nanostructure for simultaneous detection and treatment of diseases. [6]

The magnetic hyperthermia refers to a modality of cancer therapy in medical oncology in which the tumour cells are subjected to a temperature of about 40°C obtained, among others, by applying an alternating magnetic field to magnetic nanoparticles (MNP's), just iron oxides or ferrite spinels. [7] The use of these materials is favoured by their safety, cheapness and, more importantly, biocompatibility. The enormous progresses made in nanotechnology have taken MH to a much higher degree of development in these last years. For example, the application of MNP's in medicine is moving towards targeting body regions otherwise difficult to reach and to chemical manipulation at the nanoscale.

However, one of the major issues that is being investigated in magnetic hyperthermia is the reduction of the amount of MNP's to be used in living organs. [8] To this aim, the heating efficiency of MNP's should be enhanced by changing, for example, the amplitude and frequency of the external alternating magnetic field, the magnetic anisotropy, the magnetization values, the particle-particle interactions, as well as particles size and size distribution of the MNP's. For hyperthermia applications, the thermal energy dissipation in the tumour cells depend on the saturation magnetization Ms of MNP's at body temperature. Thus, higher Ms values are required in order to perform less invasive treatments. On the other hand, a high Ms allows better control on the movement of the MNP's in the blood using external magnetic field. [9] The most popular Fe_3O_4 and γ-Fe_2O_3 nanoparticles, display a large variety of M_S values depending on the particle sizes and the synthesis route, ranging between 2 and 60 emu/g, but difficulties in recognizing the pure contribution from nanoparticles are often evidenced.

A promising class of materials to be used for magnetic hyperthermia are the spinel ferrites with the general formula AB_2O_4 (A= divalent cation, such as Zn, Ni, Co; B= trivalent cation, Fe). [10-13] In particular, zinc ferrite nanoparticles earned a great deal of attention in nanomedicine mainly due to the small toxicity of Zn. This is an important request for biocompatible MRI contrast agents in the field of medical science because present contrast agents are toxic in nature. $ZnFe_2O_4$ nanoparticles have been known as good candidate for MRI contrast agents since the permissible RDI (Reference

Daily Intake) doses for Fe and Zn are 18 and 15 mg/day, respectively, much higher than any other biocompatible material. In addition, they possess interesting saturation magnetization, similar to the most used iron oxides, but with the advantage of Zn antibacteric effect and the possibility to use lower material amount in the body. On the other hand, thanks to their electric and magnetic properties, they are appealing in various other application fields, such as high-density magnetic storage and electronic communication devices and sensors. [14-16] In this frame, it is important to monitor the sample purity and to avoid the presence of unwanted iron oxides phases, [17] possible source of extrinsic contribution to the functional properties of zinc ferrites.

In the normal spinel ferrites, all the divalent and trivalent cations occupy tetrahedral and octahedral sites, respectively. The magnetic properties depend on the interactions between A and B sites and thus are very sensitive to the type of cations and their distribution in the spinel lattice. [18-19] So, the doping is used to obtain peculiar cation distribution and, in turn, optimized magnetic properties, in particular the increase of the saturation magnetization at room temperature. In the literature, among others, La, [20] Y and In, [21] Sr, [22] Al, [23] Mg, [24] Co [25-26] doped spinels were reported, showing increased superparamagnetic behaviour with respect to the undoped $ZnFe_2O_4$. Great interest could have the investigation of new kind of doping for the fine tuning of the ferrites superparamagnetism. A crucial role for high-performance nanostructured spinel ferrites is also played by the synthesis/production procedure.

In these last years, many attempts have been made to obtain particles of nanometric dimensions by using several physical and chemical experimental methodologies, including sol-gel, [27] high-energy ball milling, [28] hydro-thermal, [29] co-precipitation, [30] ultrasonic cavitation [31] and thermal plasma [32] methods. More recently, it has been observed that the microwave assisted combustion synthesis, an interesting wet chemical technique, enables fast reaction rate, chemical homogeneity and high reactivity. [20]

In this work, we report on the synthesis and characterization of $Zn_{1-x}Ca_xFe_2O_4$ (x=0.05 and 0.25) and $ZnFe_{1.9}Gd_{0.1}O_4$ prepared by using the microwave assisted combustion method. The Ca substitution is particularly interesting due to the low toxicity of the substituent; on the other side, Gd ions are commonly used as contrast agents for MRI. At our knowledge, both substitutions have never been reported in the literature. We also synthesized and characterized, for comparison, undoped $ZnFe_2O_4$ and $Zn_{0.95}Sr_{0.05}Fe_2O_4$ and $ZnFe_{1.9}Al_{0.1}O_4$ doped ferrites, these last ones not deeply investigated in the literature. A thorough characterization of structural, morphological, compositional and vibrational properties has been performed by combining X-ray powder diffraction (XRD) with the Rietveld structural refinement, Scanning Electron Microscopy with Microanalysis (SEM/EDS) techniques and micro-Raman spectroscopy. We could determine the samples purity, the lattice parameters, the crystallite sizes and, in particular, the inversion degree of

the spinel phase. The results have been discussed in view of the magnetic properties investigated by SQUID magnetometry.

2. Methods

2.1. Synthesis

The samples were synthesized by the microwave assisted combustion methodology (MW). [33] $Zn(NO_3)_2$ $6H_2O$ and $Fe(NO_3)_3$ $9H_2O$ in stoichiometric ratio were mixed with a proper amount of citric acid as fuel, as calculated from the propellant chemistry theory. [20] The mixture was placed in a microwave oven for 30 min at 800 W (the temperature in the oven was about 450-500°C). This sample will be named ZnFe. To prepare the doped samples, $Ca(NO_3)_2$ $4H_2O$, $Sr(NO_3)_2$, $Gd(NO_3)_3$ $6H_2O$ and $Al(NO_3)_3$ $9H_2O$ were added to the previous reagents to obtain the desired stoichiometry $Zn_{0.95}Ca_{0.05}Fe_2O_4$, $Zn_{0.75}Ca_{0.25}Fe_2O_4$, $Zn_{0.95}Sr_{0.05}Fe_2O_4$, $ZnFe_{1.9}Gd_{0.1}O_4$ and $ZnFe_{1.9}Al_{0.1}O_4$. In the following, these samples will be named Ca005, Ca025, Sr005, Gd01 and Al01 respectively

For comparison, an undoped $ZnFe_2O_4$ sample was also synthesized by using a standard solid state synthesis, starting from a stoichiometric mixture of ZnO and Fe_3O_4 oxides ground by ball milling in tungsten jars for 6h at 500 rpm, then treated in oven at 650°C for 12h. This sample will be named ZnFe-SS.

2.2. Characterization techniques

X-ray powder diffraction measurements were performed by using a Bruker D5005 diffractometer with the CuKα radiation, graphite monochromator and scintillation detector. The patterns were collected in air with a step size of 0.03° and counting time of 10s per step in the angular range 10-100°, by using a silicon sample holder with low background.

Rietveld structural and profile refinement was carried out by means of TOPAS 3.0 software [34] on the basis of the known crystal structure model of the cubic spinel. During the refinement, the background coefficients, scale factor, zero error, lattice parameters, isotropic thermal factors and atomic positions were allowed to vary, as well as the occupancies, to verify the possible inversion degree of the spinel. A proper constraint was used to limit the dopant amount to its stoichiometric value and to allow the inversion on the tetrahedral and octahedral sites. We also determined the crystallite sizes, an important parameter to be related to the superparamagnetic effect. The weight percentages of the impurity phases, when present, were also determined.

A Zeiss EVO MA10 (Carl Zeiss, Oberkochen, Germany) scanning electron microscope coupled with an EDS detector (X-max 50 mm^2, Oxford Instruments) was used for the morphological study and the elemental microanalysis of the samples. SEM measurements were performed on gold sputtered samples.

Micro-Raman measurements were carried out at room temperature by using a Labram Dilor spectrometer equipped with an Olympus microscope HS BX40. The 632.8 nm light from He-Ne laser was employed as excitation radiation. The samples, mounted on a motorized *xy* stage, were tested with a 100x objective and with a laser spot of ~1 μm of diameter. The spectral resolution was about 1 cm^{-1}. Neutral filters with different optical density were used to irradiate the samples at different light intensities leading to power density values from $5x10^3$ W/cm^2 to $5x10^5$ W/cm^2. A cooled CCD camera was used as a detector and the typical integration times were about 2 minutes. The sample phase homogeneity was verified by mapping the Raman spectra from different regions of each sample. The parameters of the Raman spectra were extracted by using best fitting procedures based on Lorentzian functions. In this way the frequency, full width at half maximum, intensity and integrated intensity of the peaks were determined.

The magnetic characterization was carried out by means of a SQUID magnetometer. A 100 Oe magnetic field has been applied to study the temperature dependence of the magnetization in the range 2-302 K, in zero-field cooling (ZFC) and field cooling (FC) regimes. Hysteresis loops were collected at room temperature with magnetic field ranging between 0 and ± 30000 Oe.

3. Results and discussion

3.1. XRD and Rietveld refinement

In Figure 1 the XRD patterns of the undoped $ZnFe_2O_4$ samples are shown. The peaks well agree with the $ZnFe_2O_4$ cubic spinel structure (JCPDS card N. 89-7412, franklinite mineral). In both cases, a high purity level is found. The different peaks broadening and crystallinity suggest markedly different particle sizes in the two samples, as can be expected due to the different sintering temperatures and procedures.

The patterns of doped $ZnFe_2O_4$ samples obtained from the microwave combustion synthesis are compared with the undoped one in Fig. 2. In all the cases, the experimental peaks are well explained by the $ZnFe_2O_4$ cubic spinel structure. No traces of unreacted reagents nor phase impurities are present: only for Sr005 the low peaks at about 20 and 38° reveal the presence of small traces of strontium nitrate, as a residual of the reagent. So, we can infer that all the performed doping were effective. For Ca substitution only, this synthesis procedure allowed us to introduce a significant amount of dopant in the ferrite structure. For Gd ion, in fact, all the attempts to increase the doping level up to 5 atom% failed, and the samples were constituted by a mixture of phases or were even amorphous. This could be due to the marked preference of gadolinium for high coordination number (8-9) and to the difficulty of ions to adapt to iron octahedra.

It can be seen, from the observed peak widths, that the samples show similar crystallinity degree, apart from Ca025, whose pattern exhibits broadened peaks. In any case, a value of about

1.07° for the FWHM of the peak at about 35° corresponds to nanoparticles with sizes of 8 nm, as could be estimated by using the Scherrer equation.

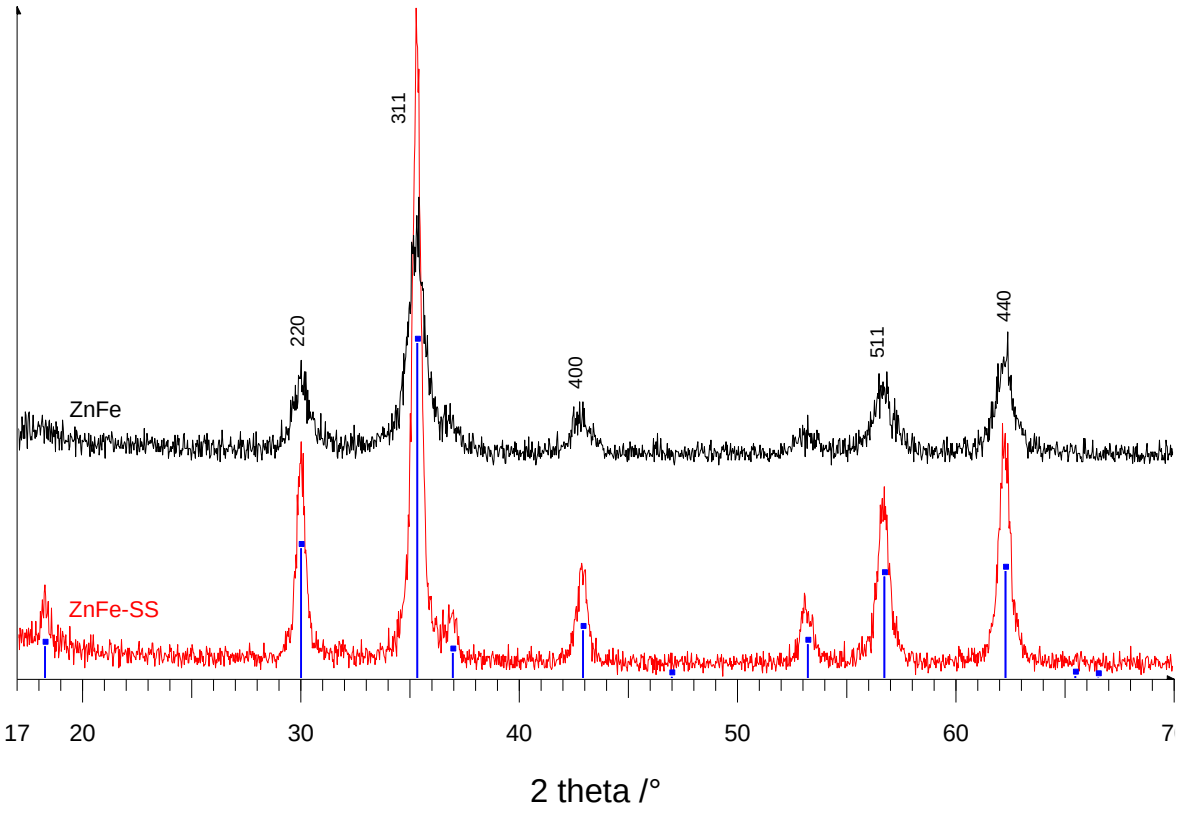

Figure 1 –XRD patterns of undoped $ZnFe_2O_4$ obtained from microwave combustion and solid state methods. The bars of the expected angular positions of the spinel phase (JCPDS card 89-7412) are also reported, together with the Miller indices of the main peaks.

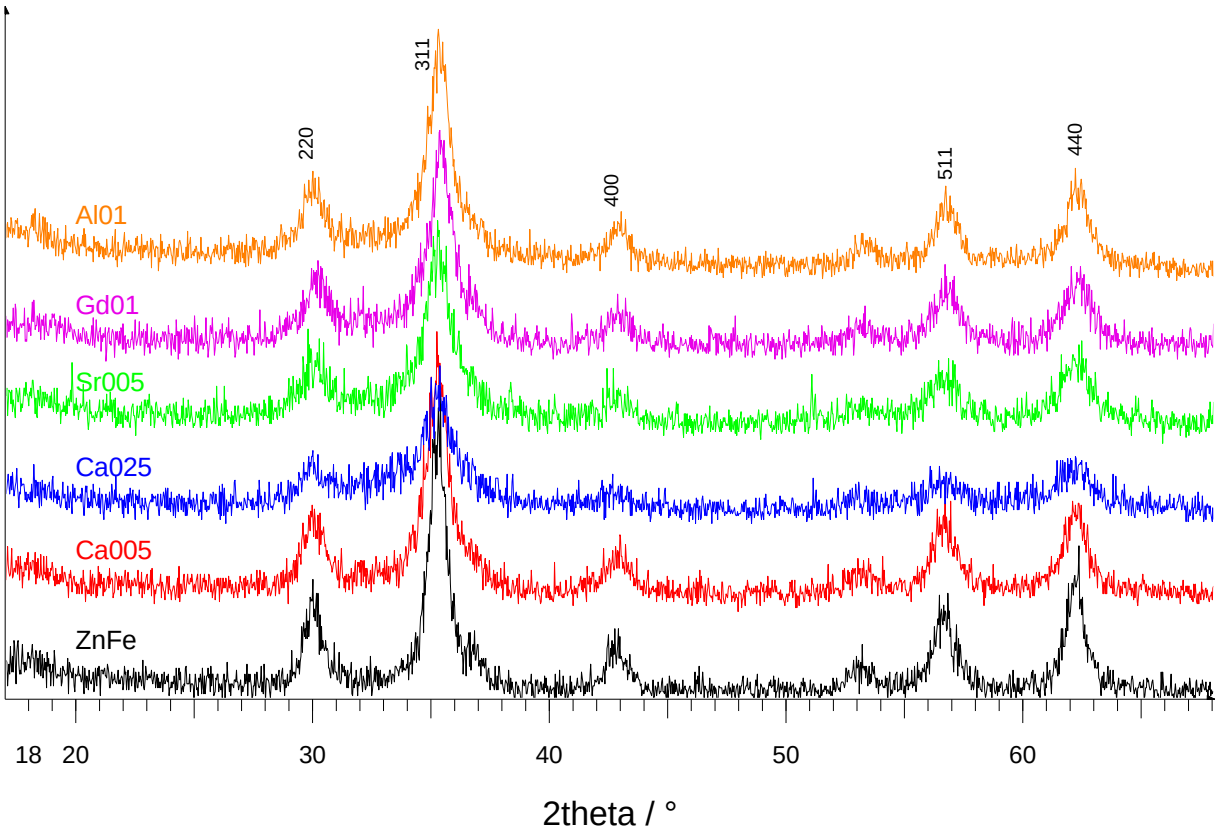

Figure 2 - XRD patterns of doped $ZnFe_2O_4$ samples obtained by microwave combustion method (ZnFe is also shown for comparison). The Miller indices of the main peaks are reported.

The structural refinement on the basis of the Rietveld method was performed on all the patterns by using the known cubic spinel model. The main refined structural parameters are reported in Table 1, together with the discrepancy factors R_{wp} and the goodness of fit S, whose values suggest a good quality of the refinement.

In Fig. 3, as an example, the comparison between the experimental (blue) and calculated (red) patterns of Ca005 sample is shown. The difference curve (gray) is almost flat, suggesting the excellent quality of the refinement.

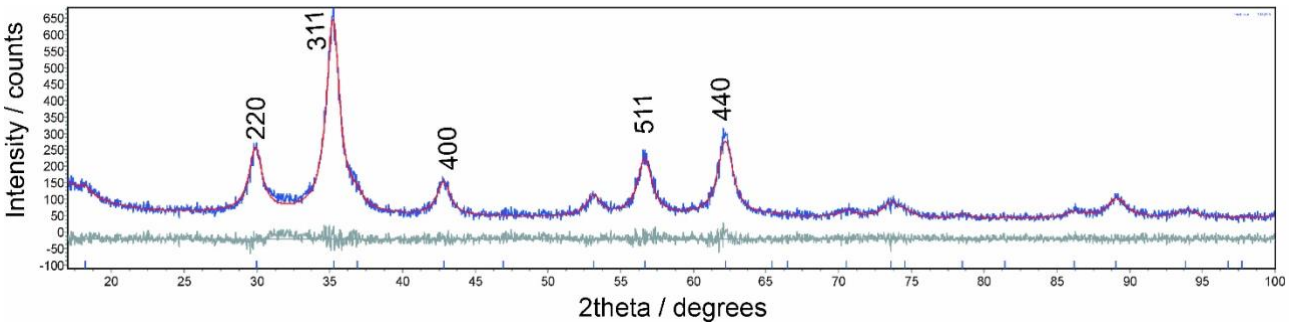

Figure 3 – Rietveld structural refinement of Ca005 sample. The Miller indices of the main peaks are also evidenced.

From Table 1 it can be seen that the crystallite sizes are all in the nanometer range: the values for the microwave synthesis are all lower than 11 nm, while for ZnFe-SS a value of 22 nm is found. In principle, the lattice parameters may vary due to the different ionic radii of the dopants with respect to Zn and Fe ions. [35] However, it seems that the most significant variation, justifiable on the basis of the ionic radii of the involved elements, only occurs for the Al doping. In this case, the cubic parameter decreases with respect to the undoped sample: in fact, a value of 0.53 Å is reported for Al^{3+} ions with respect to 0.65 Å of Fe^{3+} in high spin configuration. [35] The addition of Gd, Ca and Sr ions, whose ionic radii are larger than those of Fe and Zn, does not instead produce significant variations of the lattice parameter. On the other hand, a similar behaviour for the lattice parameter was found for the Sr substituted samples reported in ref. 22. We also determined, from the structural refinement, the inversion degree, i.e. the amount of Fe ions on Zn crystallographic sites. In all the cases, the inversion takes place, although not so markedly: only for Ca025 a value of 0.54 is reached. The easily induced inversion can be a consequence of the quickness of the MW synthesis, that in only about 30 min can produce a good level of crystallinity but with atomic disorder. We also verified by the structural refinement that the dopants are located on the sites that we supposed for the preparation of the samples. So, Ca and Sr ions seem to prefer the A site, while Al and Gd ions the B one. This is certainly true when the substitution is about 5 atom%, while for Ca025 a different model could be hypothesized. In fact, due to the preference of calcium for octahedral coordination it is possible that these ions could be also located on Fe sites, so inducing a higher inversion degree with respect to Ca005 and a small contraction of the lattice parameter.

Table 1: cation distribution, impurity phases amount, lattice parameter, crystallite size and discrepancy factors R_{wp} and S obtained from the Rietveld refinement.

	Cations distribution	Impurities	a/Å	Size/ nm	Rwp/S
ZnFe-SS	$[Zn_{0.93}Fe_{0.07}]_T[Fe_{1.93}Zn_{0.07}]_O$	-	8.4386(6)	22.9	13.80/1.07
ZnFe	$[Zn_{0.82}Fe_{0.18}]_T[Fe_{1.82}Zn_{0.18}]_O$	-	8.4371(40)	11.1	14.97/1.09
Al01	$[Zn_{0.68}Fe_{0.32}]_T[Fe_{1.58}Al_{0.1}Zn_{0.32}]_O$	-	8.4221(25)	8.4	10.89/1.07
Ca005	$[Zn_{0.90}Ca_{0.05}Fe_{0.05}]_T[Fe_{1.95}Zn_{0.05}]_O$	-	8.4343(17)	8.7	11.19/1.04
Ca025	$[Zn_{0.21}Ca_{0.25}Fe_{0.54}]_T[Fe_{1.46}Zn_{0.54}]_O$	-	8.4331(57)	5.5	13.56/1.05
Sr005	$[Zn_{0.88}Sr_{0.05}Fe_{0.07}]_T[Fe_{1.93}Zn_{0.07}]_O$	$Sr(NO_3)_2$ 3.35	8.4380(13)	7.2	11.14/1.13
Gd01	$[Zn_{0.98}Fe_{0.02}]_T[Fe_{1.88}Gd_{0.1}Zn_{0.02}]_O$	-	8.4366(29)	8.4	13.47/1.05

3.2. Morphological and compositional analysis

SEM images, reported in Fig. 4, clear up the morphological differences between the samples from MW synthesis and ZnFe-SS, giving evidence of a higher surface/volume ratio for MW samples with respect to solid-state one. From MW, rounded particles (lower than 100 nm) aggregates with large and open pores, regardless the doping ion, can be seen. This aspect can be due to the evolution of gases from nitrates and citric acid (such as NO_2 and CO_2) during the heating process in the microwave oven. For Ca025 sample (Fig. 4b), the micrograph suggests possible melting/decomposition processes and the subsequent solidification. The solid-state synthesis also leads to aggregates, but with larger rounded particles (Fig. 4g). So, from XRD and SEM measurements we could determine the same trend for crystallite and particle sizes.

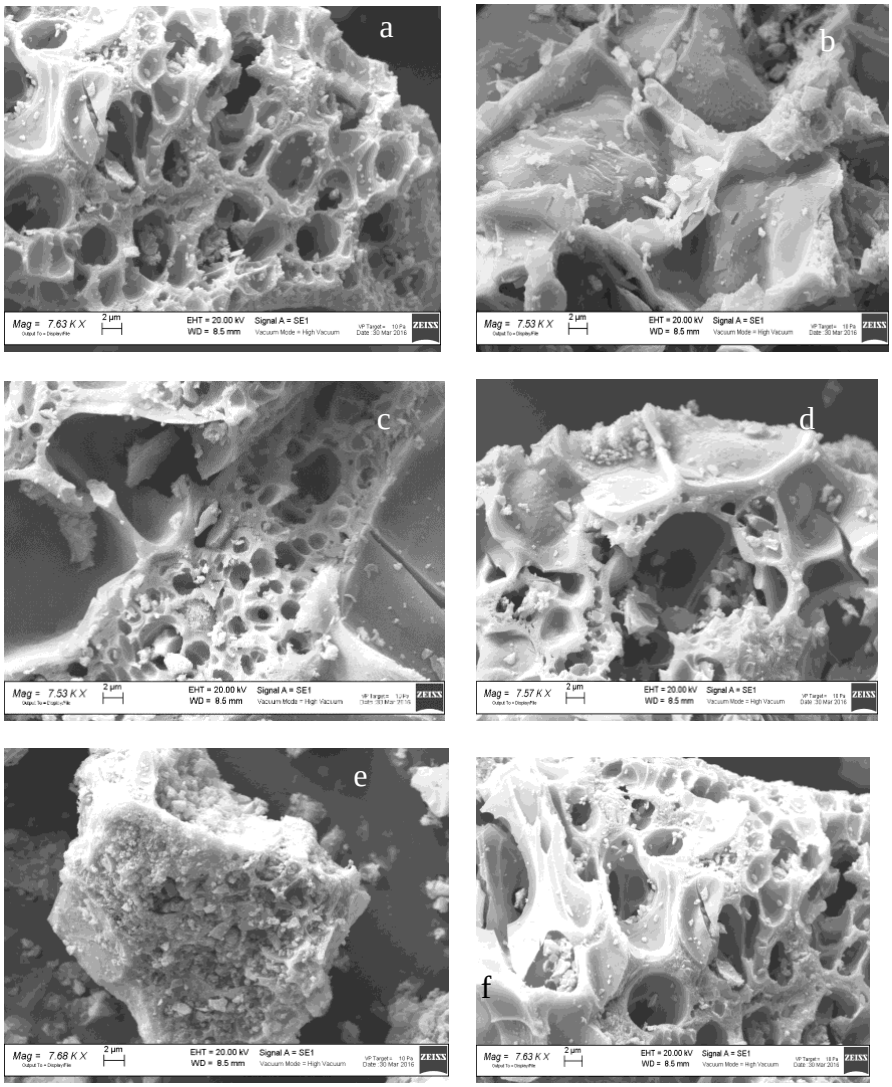

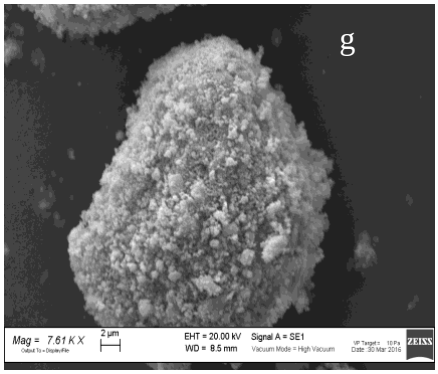

Fig. 4 - SEM micrographs of samples from MW and solid state syntheses: a) Ca005, b) Ca025, c) Sr005, d) Gd01, e) Al01, f) ZnFe and g) ZnFe-SS.

The electronic microanalysis allowed us to verify that the stoichiometric ratio between the different elements was maintained in the final products. In Fig.5, as an example, the EDS analyses of Ca025 (A) and Gd01 (B) samples are reported. The atomic percentages of all the elements are in excellent agreement with the stoichiometric values, within the EDS detection limit, suggesting that the ferrites possess the expected composition and no ions loss occurred. The maps of the different elements show good homogeneity, suggesting that both Ca and Gd ions are well distributed in the sample. A similar behaviour was observed for all the undoped and the other doped samples.

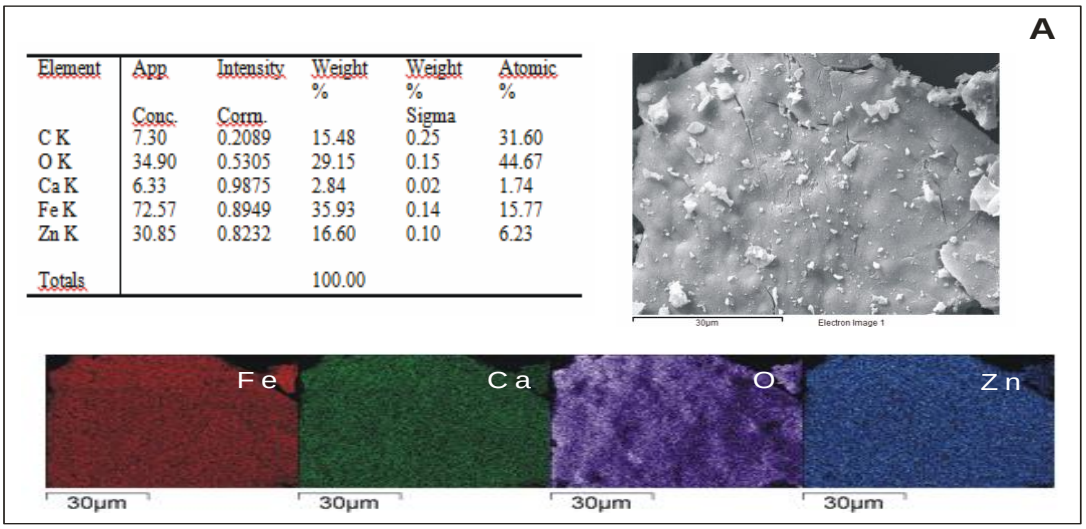

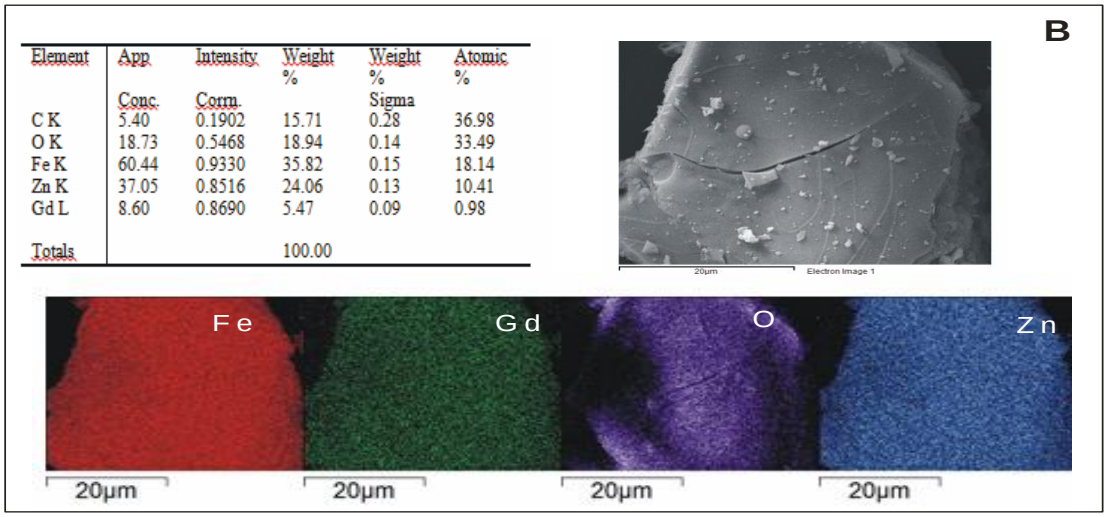

Fig. 5 – Elemental EDS analysis, the relative SEM image and the maps of the different elements for Ca025 (A) and Gd01 (B) samples.

3.3. Raman spectroscopy

Bulk $ZnFe_2O_4$ has a direct spinel structure with cubic symmetry and O7h Fd3m space group. Group theory predicts five first order Raman active modes ($A_{1g} + E_g + 3F_{2g}$) at room temperature. According to the literature, [14, 36-38] three main features appear in the room temperature spectrum of $ZnFe_2O_4$, being the most intense at about 650 cm^{-1} and the other two at about 450 cm^{-1} and 355 cm^{-1}. These signals are usually attributed to A_{1g} symmetric stretching of oxygen in tetrahedral ZnO_4 groups and to the $F_{2g}(3)$ and $F_{2g}(2)$ vibrations of octahedral FeO_6 groups, respectively. Weaker features in the low energy region are due to the E_g mode at about 250 cm^{-1} and to the $F_{2g}(1)$ translational movement of the whole tetrahedron at 160 cm^{-1}.

In Fig. 6 the Raman spectra of the undoped $ZnFe_2O_4$ samples, obtained from solid state and microwave syntheses, are reported. The most prominent signals are in agreement with the literature:

the intense feature around 650 cm^{-1} (A_{1g} mode) is accompanied by the other modes at lower energy. The lower total Raman yield and the broadening of the signals of MW sample are consistent with the lower density and smaller crystallite size of the MW powders. The reduced crystallite size (11 nm for ZnFe against 22.9 nm for ZnFe-SS) could be also responsible for the weak, but observable, red-shift for all the Raman features. For the higher energy A_{1g} mode, the peak position moves from 642.5 cm^{-1} to 638.5 cm^{-1}, while for the lower energy mode $F_{2g}(2)$ the peak is located at 345.0 cm^{-1} for ZnFe-SS sample and at 334.0 cm^{-1} for ZnFe one.

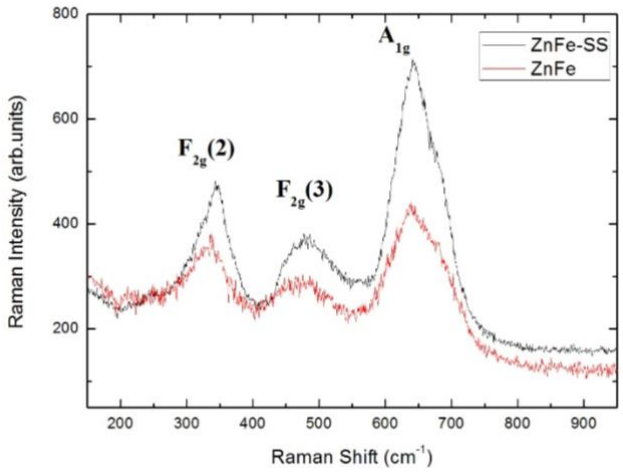

Figure 6 – Raman spectra of ZnFe and ZnFe-SS samples. The labels of the peaks are also shown.

The lattice parameter could play a role in this red shift. The changes in Raman line position due to changes in the lattice parameter can be estimated according to ref. 39 as $\Delta\omega_i = -3\,\gamma_i(q)\omega_i(q)(\Delta a/a_0)$, where γ is the Gruneisen mode parameter and $\Delta\omega_i$ is the shift of Raman line. The values of γ taken by [36] are 0.72 for A_{1g} mode and 1.88 for the F_{2g} lower energy mode. Considering the lattice parameters estimated from XRD data one should expect a Raman shift of about 2.0 cm^{-1} and 3.5 cm^{-1} for A_{1g} and F_{2g} modes, respectively. Thus, other phenomena should affect Raman frequencies, in particular the inversion degree in the spinel structure. The inversion is forced by nanometric dimension even in pure samples, as revealed in our XRD analyses and as already evidenced by several other works. [20-22] Indeed, the disorder in the cation distribution on A and B sites reflects on the broadening of Raman bands, because two different cations are involved in the vibrations inside the octahedral and tetrahedral units. In particular, concerning the A_{1g} mode, it is commonly accepted that, when the vibration is excited in FeO_4 tetrahedra produces a signal at about 690 cm^{-1}, while when it is forced in ZnO_4 the related signal is located at about 650 cm^{-1}. [40, 41] Thus, it is possible to analyse the Raman spectra using a so-called two modes (or phases) approach. In Fig. 7 the spectrum of pure ZnFe-SS sample is reported, together with the result from the best-fitting

procedure, where Lorenztian curves have been used. Due to the different involved masses, we used three couples of oscillators for the three main Raman features with an additional curve for the low energy weaker signals. A very satisfactory agreement with experimental data has been obtained.

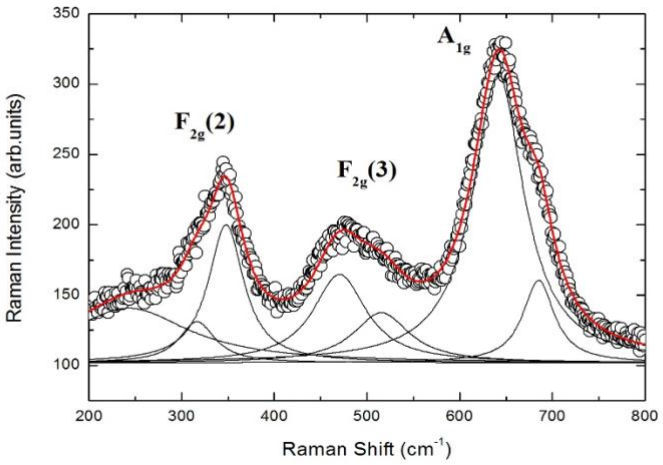

Figure 7 – Experimental and calculated Raman spectrum of ZnFe-SS sample (see text). The labels of the peaks are also shown.

In particular, the A_{1g} band is well fitted by the overlapping of two signals: the first, centred at 641 cm^{-1}, gives the main contribution and the second, centred at 685 cm^{-1}, results in a shoulder at higher energies. The energies are in good agreement with those expected for modes inside ZnO_4 and FeO_4 units. From the intensities of these bands, by applying the simple formula $I_{690}/(I_{690}+ I_{647})$, we could estimate the inversion degree obtaining, for ZnFe-SS sample, a value equal to 0.095, slightly higher than 0.07, derived from XRD analysis.

In Fig. 8a the Raman spectra in the range 200-1000 cm^{-1} of the doped samples obtained from MW synthesis are shown, in order to compare the first order Raman signals (ZnFe sample is reported for comparison). All the samples exhibit a well-defined first order Raman scattering pertinent to the ferrite phase. The substantial invariance of the Raman features for all the samples indicates a good stability of the spinel structure.

We also explored the higher energy part of the Raman spectrum. As representative cases, in Fig. 8b the spectra of Sr005 and Gd01 samples have been reported in the range 200-1800 cm^{-1}. Signals with low intensity can be detected. In particular, only for Sr005 sample, a peak centred at about 960 cm^{-1} has been observed (see arrow in Fig. 8b), probably due to $Sr(NO_3)_2$ impurity phase, also revealed by XRD. No other impurity phases have been revealed, in particular in the region of carbon modes, where only the second-order features of zinc ferrite appear at around 1100 and 1300 cm^{-1}.

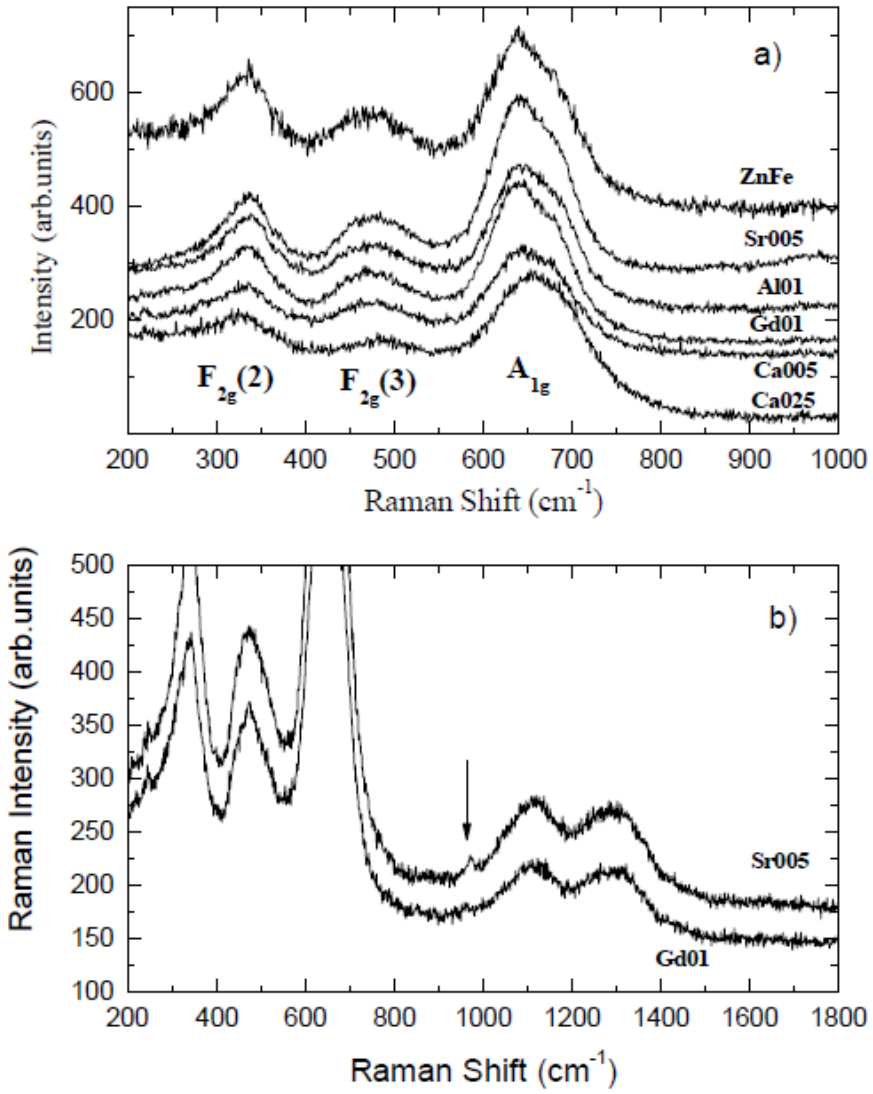

Figure 8– a) Raman spectra of the samples from MW synthesis in the range 200-1000 cm^{-1} b) representative Raman spectra of Sr005 and Gd01 samples in the range 200-1800 cm^{-1}. The labels of the peaks are also shown.

Concerning the 1st-order modes for Ca and Gd samples, a weak feature at around 220 cm^{-1}, probably due to the $F_{2g}(1)$ mode, is present. The doping doesn't markedly change the peak positions and only for the Ca025 sample a net shift is observed: the higher bands move at higher energies, while the $F_{2g}(2)$ signal further decreases in energy. The main difference among the samples concerns with the broadening of the bands, related to the amount of doping and to the crystallite sizes. Indeed, the bands of Ca025 are more broadened and this sample has the greater amount of substituent and the lower crystallite size.

As already mentioned, both doping and nanometric sizes also affect the inversion dynamic. Thus, it is important to monitor the inversion degree in all the samples. According to what described for ZnFe-SS sample, the integrated intensities of the two components of the main A_{1g} Raman feature have been derived, after averaging the results from several Raman runs. Two representative cases are reported in Fig. 9.

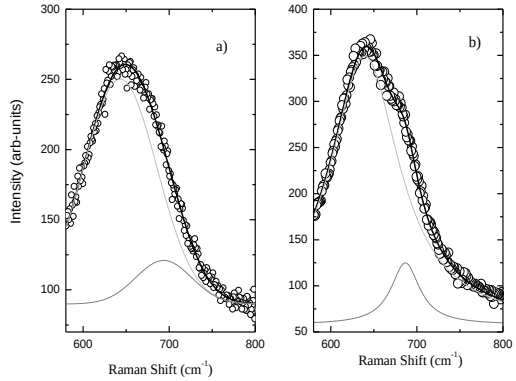

Figure 9 – Two representative examples of best fitting of the A_{1g} mode in the range 580-800 cm^{-1} for a) Ca005 and b) Gd01 samples.

The values of the inversion degree are reported in Fig. 10 in form of histogram and compared with the XRD values (Tab. 1).

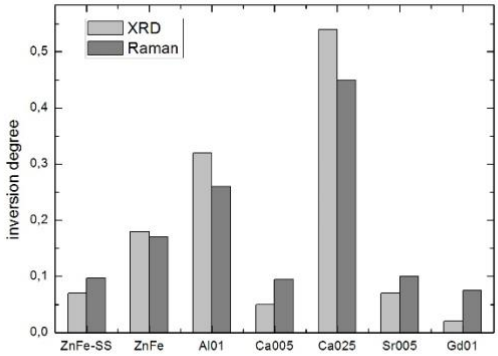

Figure 10 – Histograms showing the inversion degree obtained from Raman and XRD data as explained in the text, for all the synthesized ferrite samples.

The inversion degree derived from XRD and Raman evidences a common trend and the highest inversion is found for Ca025 with both the techniques. Absolute values from the two methods do not coincide, but it must be taken into account that the two experimental probes have a different penetration depth and thus they can experience different structural features, especially when

clustered nanometric particles are involved. Raman scattering is more sensitive to the surface, while XRD is a bulk technique, thus it is not surprising that for undoped and low-level doped samples higher inversion degree are derived from Raman measurements, because the surfaces are the most defective and disordered sample zones. On the contrary, for Al01 and Ca025 samples, a slightly higher inversion degree is derived from XRD analysis. At this purpose, we have to consider the higher doping level, with respect to other samples, and the differences in ionic radii [35] with respect to the substituted ions. In fact, Ca ions are markedly greater, while Al markedly lower than Zn and Fe ones. In addition, Ca025 powders exhibit the lower crystallite size. All these effects can lead to an increase of inversion degree in the core of nanoparticles. In addition, at higher doping level, the contribution of substituents in Raman modes can give rise to a proper vibration at a specific energy and the two Lorenztian model used to interpolate A_1g modes remain effective even with minor physical meaning and the error in inversion degree estimation can grow.

3.4. Magnetic characterization

Hysteresis cycles provide a basic proof of room temperature superparamagnetic behaviour, essential requirement in magnetic hyperthermia. Fig. 11 reports the hysteresis cycles recorded at room temperature for all the MW samples. Main common features can be inferred, referable to a superparamagnetic behaviour: negligible values of coercive field and remanence magnetization and no full saturation even at the highest applied magnetic fields, as commonly found for nanoparticles of this kind of materials. Minor differences in the curves shape can be found concerning the near-zero-field behaviour and the different tendency towards saturation. The cycle recorded in the same experimental conditions for the ZnFe-SS sample, showing the typical paramagnetic linear behaviour of the magnetization *vs* the applied magnetic field, is reported in the inset for comparison.

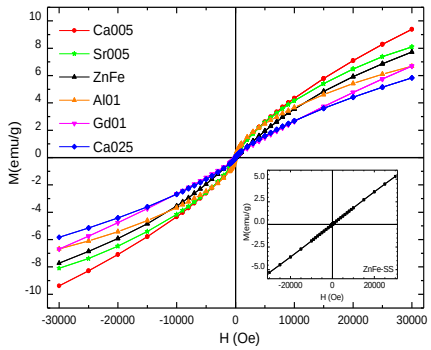

Fig. 11 – Room temperature hysteresis cycles collected from the undoped and doped $ZnFe_2O_4$ samples obtained by microwave combustion method. Inset: room temperature M *vs* H curve for the ZnFe-SS sample.

M_S values of 6-10 emu/g, when applying a 3 T magnetic field, are estimated for all our MW samples. A fair agreement is found with the M_S values reported in the literature for analogous compounds prepared by means of combustion synthesis, both pure and doped zinc ferrite spinels. For example, $Zn_{1-x}Sr_xFe_2O_4$ nanoparticles with crystallite size of about 40 nm, in the compositional range $x \leq 0.1$ show room temperature M_s values between 1.6 and 3 emu/g for the maximum applied magnetic field (1 T). [22] For $ZnFe_{2-x}La_xO_4$ (x=0.06) nanoparticles a M_S value of about 8 emu/g for ~1.4 T maximum applied magnetic field is revealed (average crystallite size of about 27 nm). [20] Undoped $ZnFe_2O_4$ samples with crystallite sizes in the range 4-12 nm show M_S values between 1.5 and 2.8 emu/g at the maximum applied magnetic field (1T). [18] Anyway, also zinc ferrite spinels obtained from different preparation techniques show, on the average, comparable M_S values. For example, the pure zinc ferrites reported in ref. 42, with crystallite sizes between 6-17 nm, show Ms values from 13.4 to 3.7 emu/g, respectively, at about 1.4 T of applied magnetic field, while values of 7 - 12 emu/g have been obtained for a 3 T applied magnetic field for Y and In doped $ZnFe_2O_4$ (particle sizes of about 4.5-8 nm), synthesized by co-precipitation method. [21]

It is well known that the spinel inversion in $ZnFe_2O_4$ promotes super exchange interactions, in turn responsible of higher M_S values with respect to the regular spinel [18, 21]. Magnetization data thus agree with the presence of spinel inversion, as determined by the XRD and Raman results.

The temperature dependence of the magnetization allowed us to draw out information about the relationships between magnetic properties and nanoparticles characteristics. The blocking temperature, T_B, representing the transition between superparamagnetic and blocked state, [4, 22] is determined by the ZFC peak position, whose broadening provides information on the particle size distribution degree, as different nanoparticles sizes give different blocking temperatures. Suggestions about spin and structural disorder of nanoparticles also come from the temperature corresponding to the merging of ZFC and FC curves, i.e. the irreversibility temperature, T_{Irr}, and its distance from T_B. [4, 43]

For ZnFe-SS, T_B and T_{Irr} merge at about 22 K, with a relatively narrow ZFC peak-width. The MW samples generally show higher T_B values and a quite marked difference between T_{Irr} and T_B. Among them, the lowest T_B value (≈32 K) pertains to Gd01, that also shows the narrowest ZFC peak-width, comparable to that of ZnFe-SS. ZFC and FC temperature dependence of magnetization for these two samples is reported in Fig. 12a. We point out that Gd01 also shows the less evident S-type shape of the superparamagnetic hysteresis loop. These features suggest that the Gd substitution on Fe site tends to prevent the structural disorder naturally induced by the MW combustion synthesis. It is

worth to observe that for Gd01 the lowest inversion degree is estimated from both Rietveld and Raman analysis (see Figure 10). For the other samples, a T_B value of about 50 K is found, a large ZFC peak-width is observed and T_{Irr} is always much higher than T_B, together with a higher level of structural and spin disorder with respect to that observed in Gd01. In particular, among the samples with substitution on Zn site (see their M *vs* T curves reported in Fig. 12b) the widest ZFC peak pertains to Ca025, that also shows the highest inversion degree, as estimated from both Rietveld and Raman analyses, confirming the relationship between structural disorder and inversion degree of the spinel. For this kind of spinels it is well known that M generally increases by decreasing grain sizes [18]. The unexpected lowest absolute value of magnetization of Ca025, observable both in M vs H and in M vs T curves, can be related to its very small grain dimensions, that, when below a critical value, can give rise to prevailing surface effects [18, 42]. Indeed, the enhanced contribution of the highly defective particle surface substantially affects the magnetic properties of the samples, [43] significantly reducing their M values with respect to the expected trend.

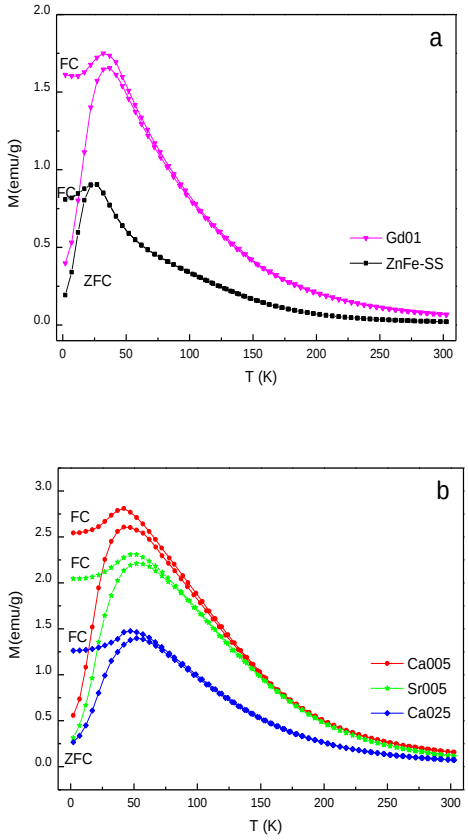

Fig. 12 – ZFC and FC M *vs* T curves at 100 Oe for (a) Gd01 and ZnFe-SS, (b) samples with substitution on Zn site.

4. Conclusions

We satisfactorily synthesized Ca and Gd doped $ZnFe_2O_4$ spinel ferrites for a proper tuning of superparamagnetic behaviour, in particular the increase of saturation magnetization at room temperature, mandatory for the biomedical application, such as magnetic hyperthermia. The microwave assisted combustion method, a rapid, green and simple synthesis route, can ensure good physical and chemical properties to the samples. An optimum purity level and homogeneity and crystallite sizes lower than 11 nm were determined for the doped samples, by the combined use of diffraction measurements with Rietveld structural refinement, SEM-EDS and Micro-Raman spectroscopy. A precise evaluation of the inversion degree of the spinel was also performed by both XRD and Raman measurements, finding a good agreement.

The hysteresis cycles showed that Ca doping ions, that have a complete solubility in the spinel structure, can induce a well evident superparamagnetic behaviour with respect to Gd ions, that instead cause a low amount of inversion and samples with almost negligible superparamagnetic characteristics. So, we can conclude that, at room temperature, the superparamagnetism is mainly due to the inversion induced by the doping in the tetrahedral site.

Acknowledgments

The authors thank Dr. Giovanna Bruni for SEM and EDS measurements.

Conflict of Interest

The authors declare no competing financial interest.

References

1 – E.A. Perigo, G. Hemery, O. Sandre, D. Ortega, E. Garaio, F. Plazaola, F.J. Teran, Fundamentals and advances in magnetic hyperthermia. *Appl. Phys. Rev.*, 2015, 041302.

2 – T. Neuberger, B. Schopf, H. Hofmann, M. Hofmann, B. von Rechenberg, Superparamagnetic nanoparticles for biomedical applications: Possibilities and limitations of a new drug delivery system. *J. Magn. Magn. Mater*., 2005, **293** 483.

3 – D. Ficai, O. Oprea, A. Ficai, A.M. Holban, Metal Oxide Nanoparticles: Potential Uses in Biomedical Applications, *Current Proteomics*, 2014, **11**, 139.

4 – A.G. Kolhatkar, A.C. Jamison, D. Litvinov, R.C. Willson, T.R. Lee, Tuning the Magnetic Properties of Nanoparticles, *Int. J. Mol. Sci*., 2013, **14**, 15977.

5- C.P. Bean, J.D. Livingston, Superparamagnetism, *J. Appl. Phys*., 1959, **30**, S120.

6- D. Yoo, J.H. Lee, T.H. Shin, J. Cheon, Theranostic magnetic nanoparticles. *Acc. Chem. Res.*, 2011, **44**, 863.

7 – A. Singh, S.K. Sahoo, Magnetic nanoparticles: a novel platform for cancer theranostics. *Drug Discovery Today*, 2014, **19**, 474.

8- P. Moroz, S.K. Jones, B.N. Gray, Magnetically mediated hyperthermia: current status and future directions. *Int J Hyperthermia*, 2002, **18**, 267.

9- I.M. Obaidat, B. Issa, Y. Haik, Magnetic Properties of Magnetic Nanoparticles for Efficient Hyperthermia. *Nanomaterials*, 2015, **5**, 63.

10- Q. Su, S. Wang, L. Yao, H. Li, G. Du, H. Ye, Y. Fang, Study on the Electrochemical Reaction Mechanism of $ZnFe_2O_4$ by In Situ Transmission Electron Microscopy. *Sci. Rep.*, 2016, **6**:28197.

11- E.R. Kumar, P.S.P. Reddy, G.S. Devi, Structural and Gas Sensing Properties of Mn Substituted $ZnFe_2O_4$ Nanoparticles by Auto Combustion and Evaporation Method. *J. Adv. Phys.*, 2016, **5**, 230.

12- S. Ameer, I.H. Gul, N. Mahmood, M. Mujahid, Synthesis, characterization and optical properties of in situ $ZnFe_2O_4$ functionalized rGO nano hybrids through modified solvothermal approach. *Opt. Mater.*, 2015, **45**, 69.

13- O.V. Yelenich, S.O. Solopan, T.V. Kolodiazhnyi, V.V. Dzyublyuk, A.I. Tovstolytkin, A.G. Belous, Magnetic properties and high heating efficiency of $ZnFe_2O_4$ nanoparticles. *Materials Chemistry and Physics*, 2014, **146**, 129.

14 – Z.Z. Lazarevic, C. Jovalekic, A. Milutinovic, D. Sekulic, V.N. Ivanovski, A. Recnik, B. Cekic, N.Z. Romcevic, Nanodimensional spinel $NiFe_2O_4$ and $ZnFe_2O_4$ ferrites prepared by soft mechanochemical synthesis. *J. Appl. Phys.*, 2013, **113**:187221

15- X. Niu, W. Du, W. Du, Preparation and gas sensing properties of ZnM_2O_4 (M = Fe, Co, Cr), *Sens. Actuators B* 2004, **99**, 405.

16- C. Qiu, M.G. Wang, Photocatalytic properties and optical absorption of zinc ferrite nanometer films, *Mater. Sci. Eng. B*, 2004, **112**, 1.

17 – X. Bo, G. Li, X. Qiu, Y. Xue, L. Li, Magnetic diphase nanostructure of $ZnFe_2O_4$/ γ-Fe_2O_3. *J. Solid State Chem*., 2007, **180**, 1038.

18- R.S. Yadav, J. Havlica, I. Kuritka, Z. Kozakova, M. Palou, E. Bartonıckova, M. Bohac, F. Frajkorova, J. Masilko, M. Hajduchova, V. Enev, J. Wasserbauer, Magnetic Properties of $ZnFe_2O_4$ Nanoparticles Synthesized by Starch-Assisted Sol–Gel Auto-combustion Method. *J Supercond Nov Magn*., 2015, **28**, 1417.

19- M. Mozaffari, M. Eghbali Arani, J. Amighian, The effect of cation distribution on magnetization of $ZnFe_2O_4$ nanoparticles. *J. Magn. Magn. Mater.*, 2010, **322**, 3240.

20- R. Tholkappiyan, K. Vishista, Influence of lanthanum on the optomagnetic properties of zinc ferrite prepared by combustion method. *Physica B,* 2014, **448**, 177.

21- M. Milanovic, E.G. Moshopoulou, D. Stamopoulos, E. Devlin, K.P. Giannakopoulos, A.G. Kontos, K. Eleftheriadis, M.I. Gini, L.M. Nikolic, Structure and magnetic properties of $Zn_{1-x}In_xFe_2O_4$ and $ZnY_xFe_{2-x}O_4$ nanoparticles prepared by coprecipitation. *Ceramics Int.,* 2013, **39**, 3235.

22- A. Manikandan, J.J. Vijaya, L.J. Kennedy, M. Bououdina, Microwave combustion synthesis, structural, optical and magnetic properties of $Zn_{1-x}Sr_xFe_2O_4$ nanoparticles. *Ceramics Int.,* 2013, **39**, 5909.

23- N.M. Deraz, Fabrication, characterization and magnetic behaviour of alumina-doped zinc ferrite nano-particles. *J. Anal. Appl. Pyrol.,* 2011, **91**, 48.

24- A. Manikandan, J. Vijaya, M. Sundararajan, C. Meganathan, L.J. Kennedy, M. Bououdina, Optical and magnetic properties of Mg-doped $ZnFe_2O_4$ nanoparticles prepared by rapid microwave combustion method. *Superlattices Microstruct.,* 2013, **64**, 118.

25- H. Bhargava, V.D. Sudheesh, J. Nehra, V. Sebastian, N. Lakshmi, K. Venugopalan, V.R. Reddy, A. Gupta, Size-dependent magnetic properties in $Cu_{0·25}Co_{0·25}Zn_{0·5}Fe_2O_4$. *Bull. Mater. Sci.,* 2014, **37**, 953.

26- G. Vaidyanathan, S. Sendhilnathan, R. Arulmurugan, Structural and magnetic properties of Co1-xZnxFe2O4 nanoparticles by co-precipitation method. *J. Magn. Magn. Mater.,* 2007, **313**, 293.

27- I. Ibrahim, I.O. Ali, T.M. Salama, A.A. Bahgat, M.M. Mohamed, Synthesis of magnetically recyclable spinel ferrite (MFe_2O_4, M = Zn, Co, Mn) nanocrystals engineered by sol gel-hydrothermal technology: High catalytic performances for nitroarenes reduction. *Appl. Catal. B,* 2016, **181**, 389.

28- G. Stefanic, S. Krehula, I. Stefanic, Phase development during high-energy ball-milling of zinc oxide and iron – the impact of grain size on the source and the degree of contamination. *Dalton Trans.,* 2015, **44**, 18870.

29- S. Diodati, L. Pandolfo, A. Caneschi, S. Gialanella, S. Gross, Green and low temperature synthesis of nanocrystalline transition metal ferrites by simple wet chemistry routes. *Nano Res.,* 2014, **7**, 1027.

30- K. Mazz, A. Mumtaz, S.K. Hasanin, A. Ceylan, Synthesis and magnetic properties of cobalt ferrite ($CoFe_2O_4$) nanoparticles prepared by wet chemical route. *J. Magn. Magn. Mater.,* 2007, **308**, 289.

31- M. Sivakumar, A. Towata, K. Yasui, T. Tuziuti, Y. Iida, A new ultrasonic cavitation approach for the synthesis of zinc ferrite nanocrystals, *Current Appl. Phys*., 2006, **6**, 591.

32- I. Mohai, L. Gal, J. Szepvolgyi, J. Gubicza, Z. Farkas, Synthesis of nanosized zinc ferrites from liquid precursors in RF thermal plasma reactor, *J. Europ. Ceram. Soc*., 2007, **27**, 941.

33- Md. Amir, A. Baykal, S. Guner, M. Sertkol, H. Sozeri, M. Toprak, Synthesis and Characterization of $Co_xZn_{1-x}AlFeO_4$ Nanoparticles. *J Inorg Organomet Polym*., 2015, **25**, 747.

34- Bruker AXS. *TOPAS V3.0: General profile and structural analysis software for powder diffraction data* (2005).

35- R.D. Shannon, Revised Effective Ionic Radii and Systematic Studies of Interatomic Distances in Halides and Chaleogenides, *Acta Cryst.,* 1976, **A32**, 751.

36. Z. Wang, D. Schiferl, Y. Zhao, H.S.C. O'Neill, High pressure Raman spectroscopy of spinel-type ferrite $ZnFe_2O_4$. *J. Phys. Chem. Solids,* 2003, **64**, 2517.

37- A. Ahlawat, V.G. Sathe, Raman study of $NiFe_2O_4$ nanoparticles, bulk and films: effect of laser power, *J. Raman Spectrosc.,* 2011, **42**, 1087.

38- S.W. da Silva, F. Nakagomi, M.S. Silva, A. Franco, V.K. Garg, A.C. Oliveira, P.C. Morais, Raman study of cations' distribution in $Zn_xMg_{1-x}Fe_2O_4$nanoparticles. *J. Nanopart. Res*., 2012, **14**:798.

39 – J.E. Spanier, R.D. Robinson, F. Zhang, S.W. Chan, I.P. Herman, Size-dependent properties of CeO_{2-y} nanoparticles as studied by Raman scattering. *Phys. Rev. B,* 2001, **64**:245407

40- D. Varshney, K. Verma, A. Kumar, Structural and vibrational properties of $Zn_xMn_{1-x}Fe_2O_4$ (x = 0.0, 0.25, 0.50, 0.75, 1.0) mixed ferrites. *Materials Chemistry and Physics*, 2011, **131**, 413.

41 – Z.Z. Lazarević, C. Jovalekić, V.N. Ivanovski, A. Rečnik, A. Milutinović, B. Cekić, N.Z. Romčević, Characterization of partially inverse spinel $ZnFe_2O_4$ with high saturation magnetization synthesized via soft mechanochemically assisted route. *J. Phys. Chem. Solids*, 2014, **75**, 869.

42 – M.K. Roy, B. Halder, H.C. Verma, Characteristic length scales of nanosize zinc ferrite, *Nanotechnology*, 2006, **17**, 232.

43 – C. Upadhyay, H.C. Verma, V. Sathe, A.V. Pimpale, Effect of size and synthesis route on the magnetic properties of chemically prepared nanosize $ZnFe_2O_4$. *J. Magn. Magn. Mater*., 2007, **312**, 271.

Highlights

- Microwave assisted combustion synthesis of Ca and Gd doped $ZnFe_2O_4$ nanoparticles
- Cation distribution determined by Raman spectroscopy and X-ray diffraction
- Superparamagnetism due to the inversion induced by the doping in tetrahedral site